Icarus 290 (2017) 1–13

Contents lists available at ScienceDirect

Icarus

journal homepage: www.elsevier.com/locate/icarus

A Wunda-full world? carbon dioxide ice deposits on Umbriel and other Uranian moons

Michael M. Sori*, Jonathan Bapst, Ali M. Bramson, Shane Byrne, Margaret E. Landis

Lunar and Planetary Laboratory, University of Arizona, Tucson, AZ 85721, USA

ARTICLE INFO

Article history:
Received 22 June 2016
Revised 28 January 2017
Accepted 28 February 2017
Available online 2 March 2017

ABSTRACT

Carbon dioxide has been detected on the trailing hemispheres of several Uranian satellites, but the exact nature and distribution of the molecules remain unknown. One such satellite, Umbriel, has a prominent high albedo annulus-shaped feature within the 131-km-diameter impact crater Wunda. We hypothesize that this feature is a solid deposit of CO_2 ice. We combine thermal and ballistic transport modeling to study the evolution of CO_2 molecules on the surface of Umbriel, a high-obliquity (~98°) body. Considering processes such as sublimation and Jeans escape, we find that CO_2 ice migrates to low latitudes on geologically short (100s–1000 s of years) timescales. Crater morphology and location create a local cold trap inside Wunda, and the slopes of crater walls and a central peak explain the deposit's annular shape. The high albedo and thermal inertia of CO_2 ice relative to regolith allows deposits 15-m-thick or greater to be stable over the age of the solar system. We conclude that Wunda, located at low latitude (7.9° S) and near the center of the trailing hemisphere where CO_2 detections are strongest, likely contains a solid CO_2 ice deposit. We discuss prospects for similar CO_2 ice deposits on crater floors on the other major Uranian moons, and predict that they are present on Ariel, Titania, and possibly Oberon (but not Miranda or smaller satellites). Such deposits have likely not been observed due to the limited nature of Voyager 2 image coverage.

1. Introduction

Voyager 2, the only spacecraft to visit Uranus, returned a wealth of data used to study the planet, its space environment, ring system, and satellites. The imaging science system camera (wavelength coverage from 0.28–0.64 μm) was particularly useful in studying the largest Uranian satellites, collecting images of large regions of the southern hemispheres of the five most massive moons: Miranda, Ariel, Umbriel, Titania, and Oberon (Smith et al., 1986). This data set has proved essential in analyses relevant to the moons' geology, including but not limited to their surface ages (Plescia, 1987a,b), orbital histories (Peale, 1988), crater morphology (Schenk, 1989), and cryovolcanic activity (Jankowski and Squyres, 1988).

No spacecraft has visited Uranus since the 1986 Voyager 2 flyby, but new investigations of the system hold the potential for scientific advancement for two reasons. Recent missions such as Cassini and New Horizons have revolutionized our understanding and intuition about the icy worlds of the outer solar system, and Earth-based spectroscopic observation campaigns have informed us about Uranian satellite surface compositions. Near-infrared observations made using the SpeX spectrograph (Rayner et al., 2003) at NASA's Infrared Telescope Facility (IRTF) revealed an asymmetry in water ice absorption bands on the classical Uranian moons, with deeper bands on the leading hemispheres (Grundy et al., 2003; 2006). This observation suggests less space weathered ice on those hemispheres, removal of water ice by sputtering on the trailing hemispheres, or burial of ice on the trailing hemispheres by another compound (Grundy et al., 2003, 2006). Such an asymmetry is not unexpected for tidally locked satellites (like the five major Uranian moons) (e.g., Grundy et al. 1999), but a more surprising result was the detection of carbon dioxide on the trailing hemispheres of Ariel, Umbriel, and Titania (Grundy et al., 2003, 2006). The results form a planetocentric trend, with CO_2 being most abundant on the second innermost large satellite (Ariel) and decreasing in abundance with distance from Uranus. Later IRTF observations confirmed these detections, and added a weak detection of CO_2 on Oberon (Cartwright et al., 2015). The innermost large satellite, Miranda, is an exception to this trend because CO_2 has not been detected on this moon (Bauer et al., 2002; Gourgeot et al., 2014), which we discuss in Section 4.3.

The planetocentric trend, along with the longitudinal preference of CO_2 at the trailing hemispheres, led Grundy et al. (2006) and

* Corresponding author.
E-mail address: michael.sori@gmail.com (M.M. Sori).

http://dx.doi.org/10.1016/j.icarus.2017.02.029
0019-1035/

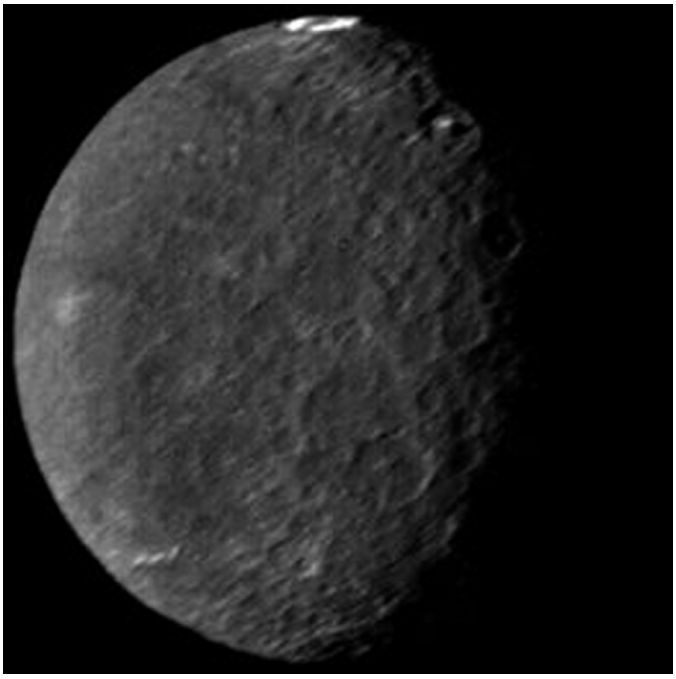

Fig. 1. Umbriel. Image 1334U2-001 taken by Voyager 2/ISS. The bright annulus inside the impact crater Wunda can be seen at the top of the picture, which is near the equator.

Cartwright et al. (2015) to favor radiolytic production of CO_2 as the primary source of this constituent. Charged particles trapped in magnetic field lines of Uranus will preferentially impinge on the trailing hemispheres of prograde moons because the field co-rotates with the planet at a faster rate than the moons' orbital periods (Ness et al., 1986). Charged particles preferentially strike the inner satellites because the magnetospheric density increases with proximity to Uranus (Stone et al., 1986). It has been shown that radiolysis can produce CO_2 if the target H_2O-rich material contains carbon (e.g., Gomis and Strazzulla, 2005), which is likely the case given the low albedo of Uranian satellite surfaces (Soifer et al., 1981; *Clark and Lucey*, 1984). An endogenic source of carbon is necessary to invoke radiolytic production because carbon ions have not been detected in the Uranian magnetosphere (Krimigis et al., 1986), and carbonaceous infall such as seen on Vesta (McCord et al., 2012) is unlikely to result in the observed longitudinal trends of CO_2 (Grundy et al., 2006). Interactions between ions caught in planetary magnetic fields and icy satellite surfaces have been documented for other bodies, e.g. Europa (Lane et al., 1981).

Umbriel (Fig. 1) is the third innermost of the five major moons of Uranus. Crater size-frequency statistics indicate it has an ancient (~4 Ga) surface, with no evidence for younger regions as there is for Miranda, Ariel, and Titania (Smith et al., 1986; *Plescia,* 1987a,b; Zahnle et al., 2003). Umbriel's surface is uniformly dark, but has one anomalously bright feature located inside Wunda, a 131-km-diameter impact crater (Smith et al., 1986; Helfenstein et al., 1989). This prominent albedo outlier is an annulus, with inner diameter ~20 km and outer diameter ~80 km. It is tempting to speculate that Wunda is filled with CO_2 ice because the feature has a high albedo, consistent with CO_2 ice, and is located on the trailing hemisphere where CO_2 was detected by previous studies (Grundy et al., 2006; Cartwright et al., 2015). This idea is consistent with the finding of (Grundy et al., 2006) that a relatively small fraction of surface area could be responsible for the CO_2 detections, and with the observation that detected CO_2 is segregated from other constituents (Cartwright et al., 2015). The possibility of a Wunda CO_2 ice deposit was briefly mentioned by (Grundy et al., 2006), but dismissed because similar features are not evident on the other Uranian moons.

In this study, we test the hypothesis that the bright feature inside Wunda is a deposit of solid, slab-like CO_2 ice. We model Umbriel's surface temperatures as a function of latitude and surface properties using a 1D thermal conduction model. These temperatures serve as inputs to a ballistic transport model, which we use to study the evolution and lifetimes of CO_2 particles on Umbriel. We include the effects of the increased albedo and thermal inertia of CO_2 ice relative to the rest of the surface, which lead to greater CO_2 ice stability, and the effect of Wunda's crater morphology, which leads to the annular shape of the bright feature. We discuss implications for the history of Umbriel and other Uranian moons, including reasons why similar features are not observed on Miranda, Ariel, Titania, and Oberon.

The approach outlined above follows studies of other airless bodies (e.g., Butler, 1997; Palmer and Brown, 2008). Transport of CO_2 on airless icy satellites has been actively observed by the Cassini spacecraft on the Saturnian satellites Rhea and Dione (Teolis et al., 2010; Teolis and Waite, 2016). Permanently shadowed cold traps with polar craters have been observed to contain ices on Mercury (e.g., Neumann et al., 2013) and the Moon (Feldman et al., 1998). However, while partial shadowing during a Uranian year (~84 Earth years) may contribute to surface temperature distributions, permanently shadowed regions analogous to polar craters on Mercury and the Moon are not possible on the Uranian satellites due to the high obliquity of the Uranian system (98°). The distribution of insolation as a function of latitude on Umbriel is critically different compared to low-obliquity bodies, and our work has implications for the transport of volatile distribution on high-obliquity bodies in general.

2. Thermal modeling

2.1. Thermal modeling methods

Voyager 2's infrared interferometer spectrometer (IRIS) derived temperatures for Uranus, Miranda, and Ariel, but could not resolve Umbriel or the other Uranian moons (Hanel et al., 1986). We thus estimate the temperatures on Umbriel by use of a thermal model. The IRIS measurements of 86 ± 1 K for southern Miranda and 84 ± 1 K for southern Ariel represent maximum temperatures because they were taken at the subsolar points on each moon, and the Voyager fly-by occurred during southern summer. We expect Umbriel's maximum temperature to be similar but slightly greater due to its darker surface. We compare our maximum modeled temperatures to the IRIS results as an approximate way to validate our model.

We use a 1D thermal model to simulate the energy balance at the surface from blackbody radiation and thermal conduction with subsurface layers, solving the heat equation with the Crank-Nicolson method (Crank and Nicolson, 1947). Using the orbital properties of Uranus and the rotation rate and pole-vector of Umbriel, we calculate solar fluxes at each latitude and local time on the moon's surface throughout a Uranian year. We assume flat terrain except for model runs that include crater geometry as discussed below. Thermal conduction is simulated by solving the thermal diffusion equation at model layer boundaries, with the top layer in radiative equilibrium and a zero flux lower boundary condition.

Parameters relevant for our models are shown in Table 1. Thermal inertia values have not been directly estimated for Umbriel. We select a nominal value of $I = 15$ J m^{-2} K^{-1} s$^{-0.5}$ for Umbrielian regolith based on observations of the thermal emission of the sur-

Table 1
List of parameters used in our thermal and ballistic transport models. Some parameters have values listed for icy regolith (marked with an r) and CO_2 ice (marked with a C).

Symbol	Parameter	Value
H_{rim}	Rim horizon height	Eq. 1
H_{peak}	Central peak horizon height	Eq. 2
D	Rim-to-rim crater diameter	131 km
d	Rim-to-floor crater depth	6.7 km
D_{peak}	Central peak diameter	20 km
h_{peak}	Central peak height	4.0 km
k	Thermal conductivity	0.00017 W m^{-1} K^{-1} (r), 0.55 W m^{-1} K^{-1} (C)
I	Thermal inertia	15 J m^{-2} K^{-1} $s^{-0.5}$ (r), 940 J m^{-2} K^{-1} $s^{-0.5}$ (C)
c	Heat capacity	837 J kg^{-1} K^{-1} (r), 1070 J kg^{-1} K^{-1} (C)
E	Eccentricity	Eq. 7
p	Vapor pressure	Eq. 4
i	Sublimation rate	Eq. 3
g	Umbriel surface gravity	0.23 m/s^2
s	Velocity probability distribution	Eq. 3
θ	Launch angle	Random between 0–90°
G	Gravitational constant	6.67e-11 m^3 kg^{-1} s^{-2}
r	Umbriel mean radius	584.7 km
ε	Emissivity	0.95 (r), 0.95 (C)
A	Bond albedo	0.1 (r), 0.5 (C)
T	Temperature	Thermal model result
μ	CO_2 molar mass	44 g/mol
M	Umbriel mass	1.17e21 kg
a	Semi-major axis	Eq. 6
d_{ball}	Travel distance	Eq. 9
k_b	Boltzmann constant	1.38e-23 J/K
R	Gas constant	8.31 J/K mol
Φ	Azimuth	Random between 0–360°
ω	True anomaly	Eq. 8

faces of the icy satellites of Saturn by Cassini's composite infrared spectrometer (Howett et al., 2010). Surfaces of icy satellites tend to have such low thermal inertias because of low surface pressures (i.e., airless) and high regolith porosity, which both decrease thermal conductivity. We use a Bond albedo of $A = 0.1$ for Umbriel's surface derived from Voyager image analysis (Veverka et al., 1987; Buratti et al., 1990) and Hubble Space Telescope observations (Karkoschka, 2001a). We assume a thermal conductivity of $k = 0.00017$ W m^{-1} K^{-1}, a surface density of $\rho = 1615$ kg m^{-3}, a heat capacity of $c = 837$ J kg^{-1} K^{-1}, and an emissivity of $\varepsilon = 0.95$ (based on values for Saturnian satellites (Howett et al., 2010)).

If sufficient CO_2 ice collects on a local region of the surface, the optical and thermal properties of CO_2 ice are used as input parameters. This would be the expected scenario for the prominent bright annulus in Wunda, if it were indeed CO_2 ice. For these cases, we assume $A = 0.5$, $\varepsilon = 0.95$, $k = 0.55$ W m^{-1} K^{-1}, $\rho = 1600$ kg m^{-3}, and $c = 1070$ J kg^{-1} K^{-1}, resulting in a thermal inertia of $I = 970$ J m^{-2} K^{-1} $s^{-0.5}$. This thermal inertia is a conservative choice with regards to ice stability because it is likely that thermal conductivity of solid CO_2 increases at the low temperatures found in the Uranian system (Sumarokov et al., 2003). Amorphous CO_2 ice may have different thermal properties but is not expected at temperatures relevant on Umbriel (Escribano et al., 2013). The albedo choice is within the allowable range of CO_2 ice reflectivities (Wood et al., 1971) and the measured albedo of Wunda's bright deposit (Smith et al., 1986). We will argue that choosing other allowable CO_2 ice albedos does not alter our conclusions (see Section 4.1).

Another complexity that may be important is crater morphology. Impact craters may be sites of preferential volatile accumulation on some planetary surfaces (e.g., Banks et al., 2010). Although not well-resolved in the Voyager imagery, we expect Wunda to be a complex crater with a central peak based on its size (Schenk, 1989). This expectation is strengthened by Cassini observations: Dione, a moon of Saturn with comparable density and surface gravity to Umbriel, has impact craters of similar diameters to Wunda (e.g., the ~140 km diameter crater Dido) that have clearly resolved central peaks (Moore et al., 2004). The geometry of a complex crater with a central peak has three relevant thermal effects. First, the sloping sides of the crater walls and peak experience different insolation. This effect can be a warming or cooling effect depending on the orientation of the slope. Second, the crater walls and peak may provide shade to the adjacent crater floor. This effect is a cooling effect because it blocks direct insolation. Third, reflected sunlight and thermal emission from the walls and the central peak may be important. This effect is a warming effect because it provides additional incoming radiation. Whether these three effects cumulatively result in net warming or cooling for different parts of Wunda requires careful thermal modeling.

The annular shape of Wunda's bright deposit could be the result of the crater's complex morphology, where the dark center represents the central peak. In this case, the base of the central peak has a diameter equal to the inner radius of the annulus, ~20 km (Smith et al., 1986). Such a size is comparable to that of Herschel on Saturn's moon Mimas, a 135-km-diameter impact crater with a depth of 10–12 km, a central peak height of 6–8 km, and a central peak base diameter of 30 km (Moore et al., 2004). We expect topographic relief of Wunda to be less than that of Herschel on the basis of photoclinometry measurements of Saturnian and Uranian satellites (Schenk, 1989). To obtain a simple estimate of Wunda's geometry, we scale down the Herschel depth values by 2/3, in accordance with the 20 km vs. 30 km values of central peak base diameters. We perform thermal model simulations for a complex crater at Wunda's location with a diameter of 131 km, a depth of 6.7 km, a central peak base diameter of 20 km, and a central peak height of 4 km. We discuss the effects of uncertainties in crater dimensions in Section 4.1. These dimensions yield wall slopes of 14.7°; the fact that other icy satellites with topographic observations have similar crater wall slopes (Bray et al., 2008) lends confidence to our estimates.

In addition to the slopes of the crater wall and central peak receiving a different incidence angle of incoming sunlight, the topog-

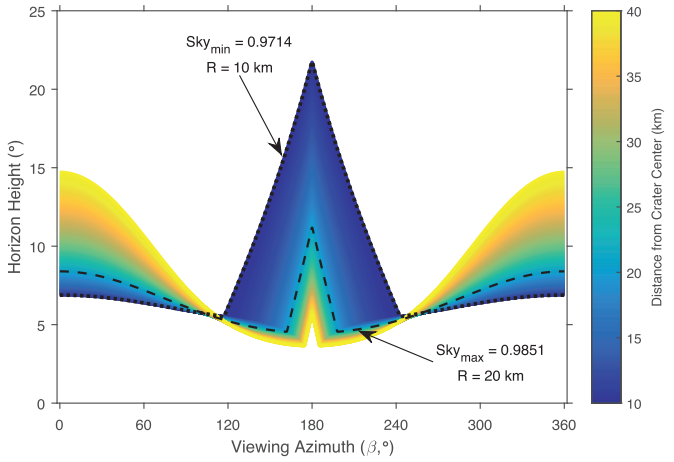

Fig. 2. Horizon height as seen from Wunda's floor as a function of viewing azimuth for various distances along a line spanning from the crater center to the north crater wall. The dotted and dashed lines show the distances where the fraction of sky unobstructed by topography is at a minimum and maximum, respectively. The peak in horizon height centered at $\beta = 180°$ (i.e., facing south) represents the effect of the crater's central peak, while the peak centered at $\beta = 0°$ (i.e., facing north) represents the effect of the crater rim.

raphy can provide shade to parts of the crater floor and exchange reradiated heat with the crater floor. To quantify these effects, we must calculate the horizon height at each point of interest on the crater floor. The horizon height due to the crater rim H_{rim} for an observer at any given point on the crater floor (x, φ in polar coordinates where north of center is $\varphi = 0$ and φ increases clockwise), facing a particular direction β (angle an observer on the crater floor is facing clockwise-relative to north), is given by:

$$H_{rim} = \arctan\left(\frac{d}{x} \times \frac{1}{\cos(\pi - \varphi + \beta) + \sqrt{\frac{D^2}{4x^2} - \sin^2(\pi - \varphi + \beta)}}\right) \quad (1)$$

D is the rim-to-rim crater diameter, d is the rim-to-floor crater depth. Similarly, the horizon height due to the central peak H_{peak} is given by:

$$H_{peak} = \arctan\left(\frac{h_{peak}}{D_{peak}} \times \frac{D_{peak} - 2x\sin(|\pi - \varphi + \beta|)}{x\cos(|\pi - \varphi + \beta|)}\right) \quad (2)$$

D_{peak} is the central peak diameter, h_{peak} is the central peak height (set to 0 when $|\pi - \varphi + \beta| > \arcsin(D/2x)$ to avoid negative values). Eqs 1 and 2 are derived in Appendix A. For any given location on the crater floor (x and φ) and direction (β), the appropriate horizon height to consider is whichever of H_{rim} and H_{peak} is greater. Horizon heights are used to calculate if a particular location is shadowed at any given time step in the thermal model, and if so, we set solar insolation to zero.

For a surface with topography, portions of the sky may be obstructed. Thus, not all emitted radiation escapes to space; some of it is exchanged with surrounding topography. We integrate horizon heights over all β (0–360°) to obtain the fraction of sky that is unobstructed to the observer (Fig. 2). For cases on sloped terrain (the crater walls or central peak), the obstructed portions of the sky were set to radiate as a surrounding flat surface, modeled independently. Surrounding terrain additionally reflects some solar radiation that we add to the direct solar radiation. The shadowing and reradiation effects described in the previous two paragraphs are cooling and warming effects, respectively.

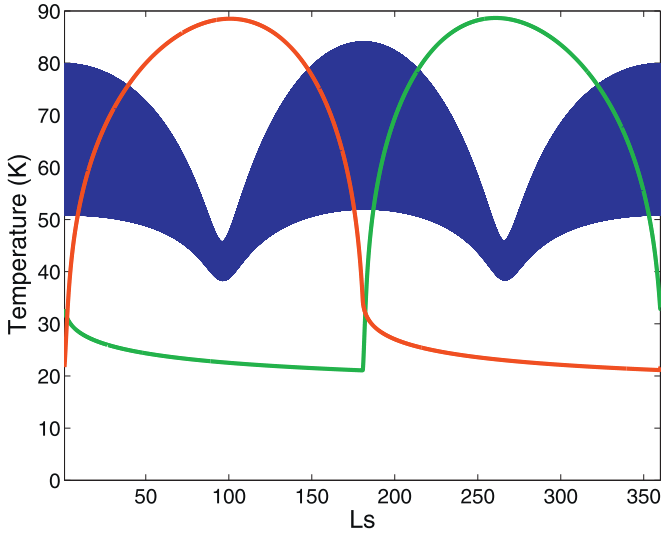

Fig. 3. Temperature results throughout one Uranian year for Umbriel's surface at the equator (blue), north pole (red), and south pole (green). Thickness of the lines represent diurnal variations. $L_S = 0$ corresponds to spring equinox. (For interpretation of the references to colour in this figure legend, the reader is referred to the web version of this article.)

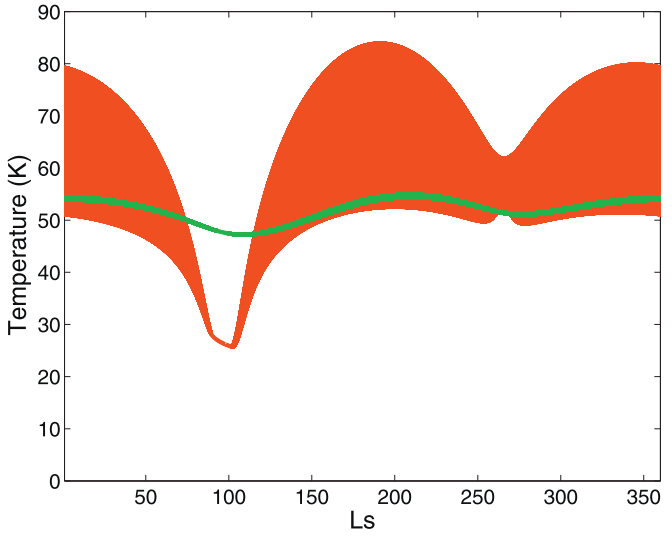

Fig. 4. Temperature results throughout one Uranian year at Wunda's latitude (7.9° S) for a surface with no topography and the thermal properties of regolith (red) and a surface with no topography and the albedo and thermal inertia of CO_2 ice (green). $L_S = 0$ corresponds to spring equinox. (For interpretation of the references to colour in this figure legend, the reader is referred to the web version of this article.)

2.2. Thermal modeling results

Resulting output temperatures for the thermal properties of regolith on a sphere of Umbriel's radius (i.e., effects of topography are not included) are shown in Fig. 3. Note the maximum temperatures (~90 K) are close to the IRIS results of Hanel et al., (1986), supporting the validity of our model. When simulating regolith temperatures, we use these thermophysical properties at all depths. Buried layers of ice at depths of 0.5 and 5 m were found to have no detectable effect on surface temperature results. As discussed in Section 2.1, if Wunda's annulus represents a deposit of CO_2 ice, it has different thermal properties and thus temperatures. Fig. 4 shows surface temperatures throughout a Uranian year for flat terrain at Wunda's location (7.9° S, 273.6° E) under both sets of thermal properties (dark regolith and CO_2 ice). The

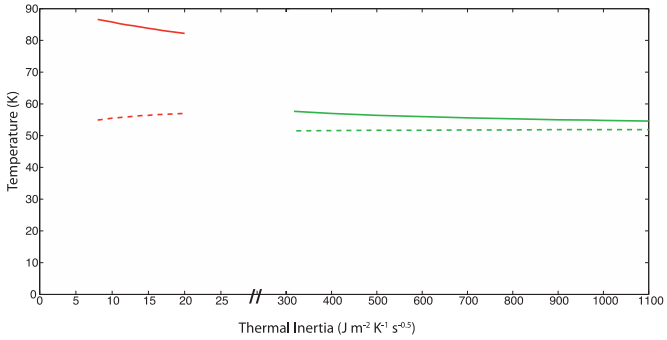

Fig. 5. Sensitivity of thermal model results to thermal inertia. Maximum (solid lines) and mean (dashed lines) temperatures throughout a Uranian year for flat topography at Wunda's latitude (7.9° S) for cases of regolith (red) and CO_2 ice (green). The break in *x*-axis is for clarity, as thermal inertia values in the missing intermediate domain are unlikely to represent regolith or ice. (For interpretation of the references to colour in this figure legend, the reader is referred to the web version of this article.)

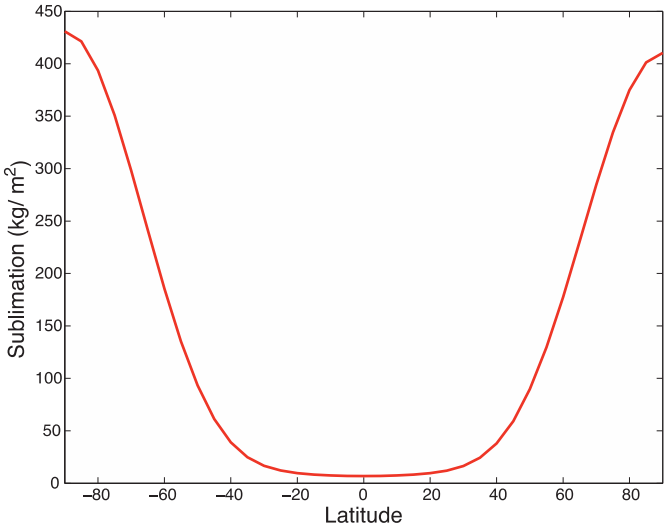

Fig. 6. Total sublimation of CO_2 ice per m^2 in a Uranian year as a function of latitude on a surface with the albedo and thermal properties of icy satellite regolith. Total sublimation for cases with the albedo and thermal properties of CO_2 ice are 7–9 orders of magnitude less and do not appear in the Fig..

presence of a CO_2 ice deposit suppresses local maximum temperatures by ~30 K. This finding is similar to the effect that ices have on local temperatures on Pluto (Earle et al., 2016), but the temperature difference is greater in our model because we took into account both the increased albedo and thermal inertia of ice deposits, whereas (Earle et al., 2016) focused on studying the effects of variable albedo.

We discuss the effects of uncertainties in model parameters on our conclusions in Section 4.1, but thermal inertias are especially uncertain due to the lack of observationally derived values for any Uranian moon and deserve quantitative consideration. We perform sensitivity tests on the values we list above (and in Table 1) by running thermal models for a range of thermal inertias. Best-fit thermal inertia values derived by (Howett et al., 2010) for large Saturnian satellites range from 8 J m^{-2} K^{-1} s$^{-0.5}$ (for Rhea's trailing hemisphere) to 20 J m^{-2} K^{-1} s$^{-0.5}$ (for Iapetus' trailing hemisphere), so we test values within this range around our nominal value of 15 J m^{-2} K^{-1} s$^{-0.5}$. We similarly test a range of values for the thermal inertia of CO_2 ice, from 300–1100 J m^{-2} K^{-1} s$^{-0.5}$ around our nominal value of 970 J m^{-2} K^{-1} s$^{-0.5}$. Thermal inertia is a function of thermal conductivity, material density, and heat capacity; our test effectively measures the sensitivity of results to conductivity because it is generally the least constrained of these three parameters. Results of our sensitivity test are shown in Fig. 5. Because sublimation rate increases rapidly with temperature, we plot the maximum annual temperature in addition to the annual-average temperature for each case. Maximum temperature only varies between 86.6–82.2 K as the thermal inertia varies between 8–20 J m^{-2} K^{-1} s$^{-0.5}$ for regolith and between 57.8–54.6 K as thermal inertia varies between 300–1100 J m^{-2} K^{-1} s$^{-0.5}$ for CO_2 ice.

We use surface temperature results to predict sublimation rates of hypothetical surface ice. Sublimation rate i is a function of the vapor pressure p, temperature T, Boltzmann constant k_b, and molecular mass μ of CO_2:

$$i = p\sqrt{\frac{\mu}{2\pi k_b T}} \tag{3}$$

The vapor pressure of CO_2 at temperature T is given by the Clausius–Clapeyron relation:

$$p = 101.3e^{23.102-\frac{3148.0}{T}} \tag{4}$$

Although experimental data measuring the vapor pressure of CO_2 are only available down to temperatures of ~150 K, theoretical work suggests it is reasonable to extrapolate empirical relations to the lower temperatures found on Umbriel (Azreg-Aïnou, 2005). Using Eqs. 3 and 4, we calculate the sublimation rate of CO_2 ice throughout a Uranian year at every 5° of latitude. We integrate these sublimation rates through time to estimate the total amount of CO_2 sublimated on Umbriel's surface in one Uranian year.

Annual sublimation results, for a perfect sphere with no topography and the thermal properties of regolith, are shown in Fig. 6. Such a set-up, also used in some of our ballistic transport models (Section 3), describes an Umbrielian surface where small grains of CO_2 ice are everywhere mixed into the regolith. This is likely not a realistic scenario for present-day Umbriel, and the absolute values of our model results describing the CO_2 budget as a function of location may not be correct. Instead, we argue that our model results use these sublimation rates to accurately describe the relative sources and sinks of CO_2 across Umbriel's surface. We additionally calculate sublimation rates for solid, slab-like CO_2 ice ($A = 0.5$ and $I = 940$ J m^{-2} K^{-1} s$^{-0.5}$) at Wunda's location and find them to be 7–9 orders of magnitude less than sublimation rates for the regolith case. This large decrease in sublimation is due to a much lower maximum temperature: ~55 K for CO_2 ice compared to ~85 K for regolith at this location (Fig. 4).

Our thermal inertia sensitivity test (Fig. 5) indicates that at Wunda's location, total sublimation in one Uranian year varies between 24.8–3.3 kg/m^2 as thermal inertia varies between 8–20 J m^{-2} K^{-1} s$^{-0.5}$ for regolith and between 1.5×10^{-6} – 2.1×10^{-7} kg/m^2 as thermal inertia varies between 300–1100 J m^{-2} K^{-1} s$^{-0.5}$ for CO_2 ice.

3. Ballistic transport

3.1. Ballistic transport methods

We use a ballistic transport model to understand the fate and evolution of sublimated CO_2 molecules, similar to an approach used to study CO_2 on Iapetus (Palmer and Brown, 2008). We assume that when a molecule sublimates at a particular time step, it takes a single suborbital hop on a ballistic trajectory and that sublimated molecules do not collide. We neglect effects of solar radiation pressure on particles. The destination of a sublimated molecule is therefore determined by its initial location, velocity, and direction. These assumptions are similar to those of Palmer and Brown (2008).

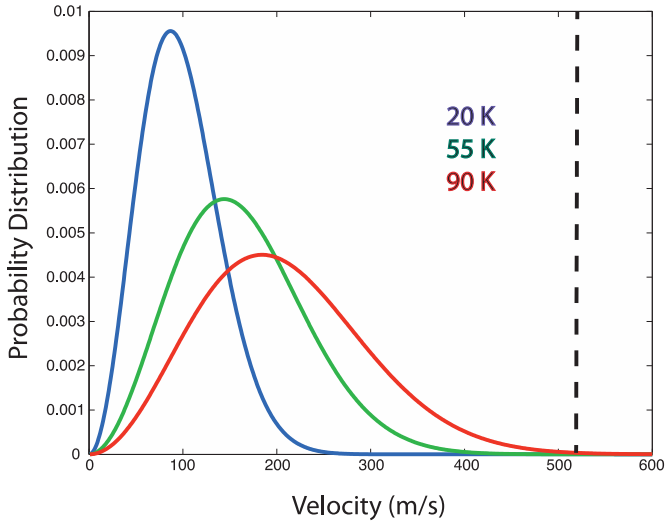

Fig. 7. Velocity distributions of sublimated CO_2 molecules on Umbriel at three different temperatures. 20 K and 90 K are the approximate minimum and maximum temperatures we calculate on Umbriel. Vertical dashed line represents Umbriel's escape velocity.

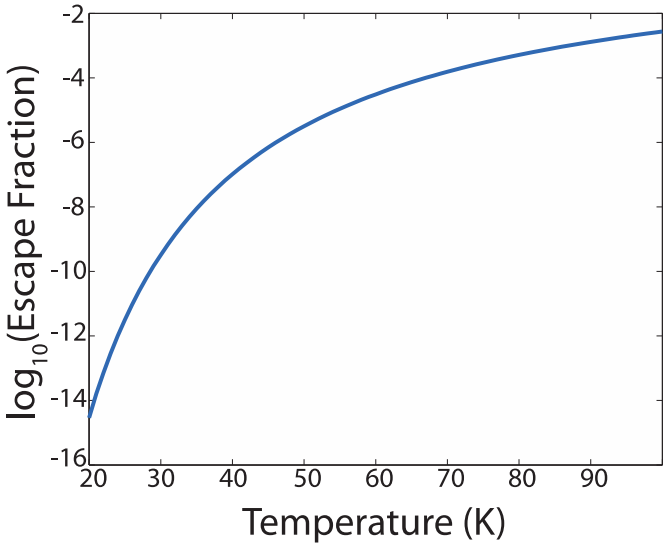

Fig. 8. Fraction of sublimated CO_2 molecules that escape Umbriel via Jeans escape as a function of temperature. Note the logarithmic *y*-axis.

We assume the distribution of initial directions is isotropic. That is, the launch angle θ at which a molecule leaves the surface relative to horizontal is randomly chosen from values between 0°–90° (weighted towards low angles with a cos θ term to keep the distribution isotropic), and the azimuth Φ is randomly chosen from values between 0°–360° (uniformly). The initial velocity v is chosen from a half-Maxwell-Boltzmann probability distribution s and is a function of the temperature T, molecular mass μ, and Boltzmann constant k_b:

$$s = 4\pi \left(\frac{\mu}{2\pi k_b T}\right)^{1.5} v^2 e^{\frac{-\mu v^2}{2k_b T}} \tag{5}$$

We show these velocity distributions for a few relevant temperatures on Umbriel in Fig. 7. The launch angle θ and velocity distribution s can be modified to include the effects of surface roughness, but this effect has been shown to be minimal and so we choose θ and s as described above (Butler, 1997). The distance d_{ball} a sublimated molecule travels is found using orbital parameters of the molecule's path: the semi-major axis a, the eccentricity E, and the true anomaly ω. These parameters are a function of the gravitational constant G, the mass of Umbriel M, the radius of Umbriel r, and the initial direction and velocity:

$$a = \frac{1}{\frac{2}{r} - \frac{v^2}{GM}} \tag{6}$$

$$E = \sqrt{1 - \frac{r(2a - r)\sin^2\phi}{a^2}} \tag{7}$$

$$\omega = \arccos\left(\frac{a - aE^2 - r}{rE}\right) \tag{8}$$

$$d_{ball} = (2\pi - 2\omega)r \tag{9}$$

We calculate the landing point of each sublimated CO_2 molecule using these equations.

We consider the loss of CO_2 molecules from Umbriel via Jeans escape. The escape velocity of Umbriel, given by $\sqrt{2gr}$, is 517 m/s. If a CO_2 molecule in our simulation is assigned a velocity $v > 517$ m/s from the velocity distribution s, we remove it from the system and assume it is permanently lost. In Fig. 8, we show the fraction of sublimated molecules that escape via this mechanism as a function of temperature.

3.2. Ballistic transport results

We combine the temperature results from our thermal model (Section 2.2) with our ballistic transport method to simulate the evolution of CO_2 ice over Umbriel's surface. In our most basic model, we assume Umbriel's surface has the thermal properties of regolith and no relevant thermal effects from topography. We take a Monte Carlo approach to determine the distribution of landing locations of sublimated molecules for a particular starting location and temperature. We simulate 10^5 sublimated molecules at every 5° of latitude for the temperatures that latitude experiences at some point throughout a Uranian year, according to our thermal results. Using Eqs 5–9, we tracked the latitude where each of these 10^5 molecules landed. We then walked through time steps of 5000 seconds at every 5° of latitude and sublimated the appropriate amount of CO_2 at each latitude and time step according to Eqs 3–4, using our distribution of the destinations of sublimated molecules to determine the ending locations of sublimated CO_2. This time step is sufficient to resolve diurnal temperature variations (an Umbrielian day is ~350,000 s), but coarser than the average flight time of sublimated molecules (~1000 s) so that molecules are unlikely to require several time steps to complete their trajectories. We kept track of the net change in CO_2 at every 5° of latitude throughout this process and integrated the results throughout one Uranian year to calculate the annual CO_2 budget for the entire moon. These results are shown in Fig. 9a.

Our results show that CO_2 ice mixed with dark Umbriel regolith is rapidly depleted from the polar regions. Latitudes greater than 50° experience a net loss of CO_2 and latitudes less than 50° experience a net gain of CO_2. Regions at a latitude of 35° experience the largest gain of CO_2 but this is a result of our initial condition of uniform CO_2. Low latitudes experience the least amount of annual sublimation, but are farthest from the polar regions that are the biggest sources of CO_2.

We performed the same simulation, but with an initial condition where CO_2 was already depleted from latitudes greater than 50° Results from this simulation reveal that the latitudes that experience a net gain of CO_2 narrow over time as expected (Fig. 9b). Further simulations of this type show that as the initial source region is narrowed in latitude, the preferred latitude for CO_2 is the equator. CO_2 is rapidly mobilized toward very low latitudes on Umbriel over geologically short timescales (kyrs). Simulations with an

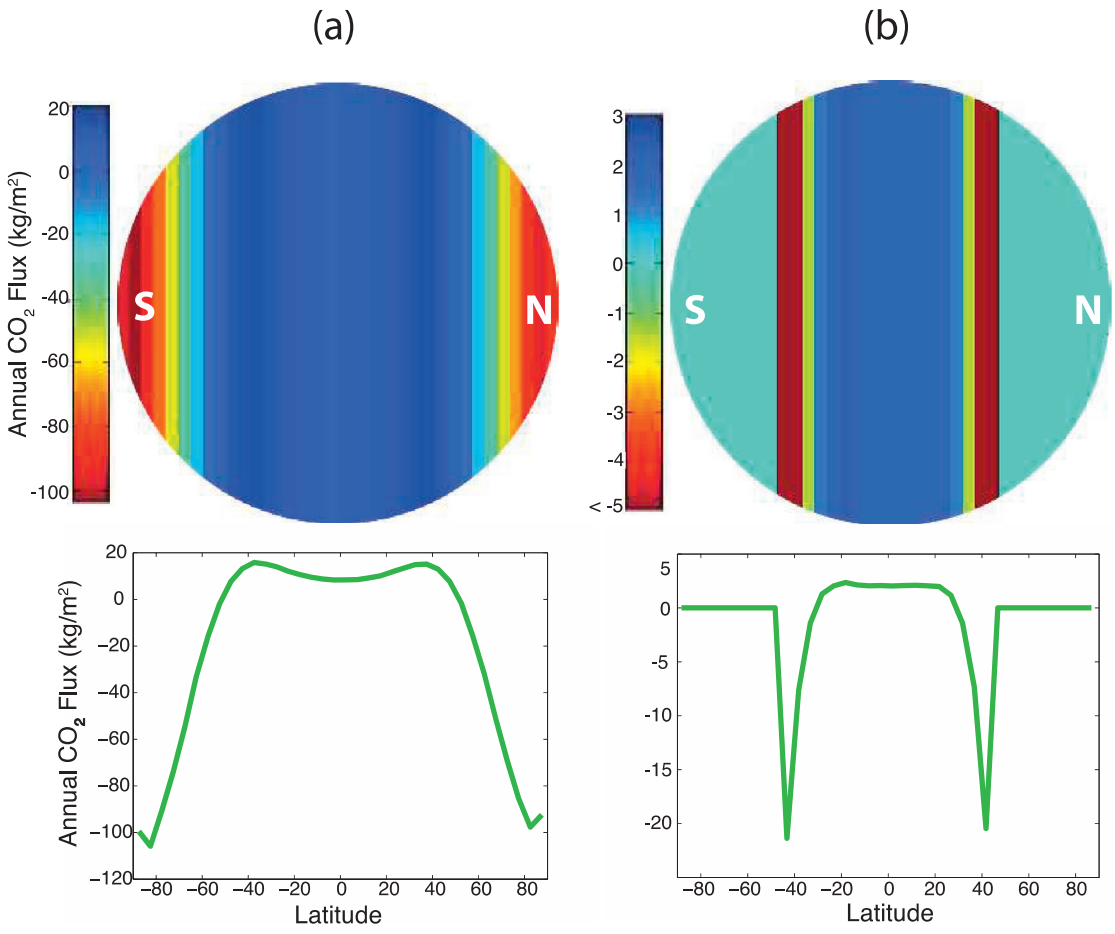

Fig. 9. Net CO2 ice flux per m^2 in a Uranian year across Umbriel with no topography (the effects of complex crater topography are shown in Fig. 10). Top row depicts the fluxes on Umbriel's surface; the south and north poles are labeled with an S and N respectively. Bottom row displays the same results, but simply as a function of latitude. (a) is for an initial condition of CO_2 ice everywhere on a surface with the properties of Umbriel regolith. (b) is the same as (a), but the initial condition only has CO_2 ice equatorward of 50°, i.e. after the polar regions have been depleted. Note the different scales in (a) vs. (b) and the narrower region of positive flux; CO_2 migrates towards the equator over time, and polar regions are not sinks for CO_2.

initial condition of CO_2 ice only mantling the trailing (where it would be produced by radiolysis) or leading hemisphere have the same behavior as shown in Fig. 9, but with the resulting CO_2 distribution concentrated in the initial hemisphere.

We consider an additional case similar to the ones above, but with a complex crater at Wunda's location with the morphological parameters described in Section 2. We use the same technique described above. Note there is no longer longitudinal symmetry in this model, and in contrast to the results shown in Fig. 9, results may vary for locations at the same latitude. These results are shown in Fig. 10. CO_2 fluxes are calculated at 40 points throughout the crater: for each of 8 directions (N, NE, E, SE, S, SW, W, and NW) we calculate the flux for a point midway up the crater wall, a point midway up the central peak, a point on the crater floor at the base of the central peak, a point on the crater floor at the base of the crater wall, and a point halfway between those two floor points. In Fig. 10, the flux results on the crater wall and central peak are interpolated in a nearest-neighbor sense, and results on the crater floor are interpolated with triangulation-based linear interpolation.

Because our initial condition of CO_2 distributed everywhere on Umbriel in large quantities is an idealized case, it is important to interpret the fluxes in Fig. 10 in a relative sense. The floor of Wunda is a relative sink of CO_2 compared to the flat terrain surrounding it (Fig. 10b); the cooling effect of shadowing slightly exceeds the warming effect of reradiation from surrounding topography. The crater walls and central peak are relative sources of CO_2 compared to flat terrain (both on the crater floor and otherwise). Maximum temperatures on Wunda's walls and central peak are only ~1.5 K warmer than maximum temperatures on the crater floor, but integrated over a Uranian year, the slight temperature difference can lead to a factor of ~2 difference in sublimation (for the most extreme case: the poleward facing side of the central peak vs. the coldest part of the crater floor). The crater floor experiences ~8% less sublimation than flat terrain just outside the crater. These effects could provide an explanation for the annular shape of Wunda's bright deposit.

Wunda may be a preferred site of CO_2 deposition compared to other low-latitude complex craters due to its proximity to the center of the trailing hemisphere, where CO_2 may be most efficiently produced by radioalysis. Wunda's bright deposit contains a low-albedo streak in its southern half (Fig. 1). Although our results reveal that the northern crater floor is slightly favored for CO_2 deposition compared to the southern crater floor, this effect is very minor, and it is more likely that topography not accounted for in our idealized simulations causes the low albedo streak.

4. Discussion

4.1. Evolution of wunda's bright deposit

We have shown that CO_2 ice migrates quickly toward the equator on Umbriel, but total sublimation per Uranian year is still high

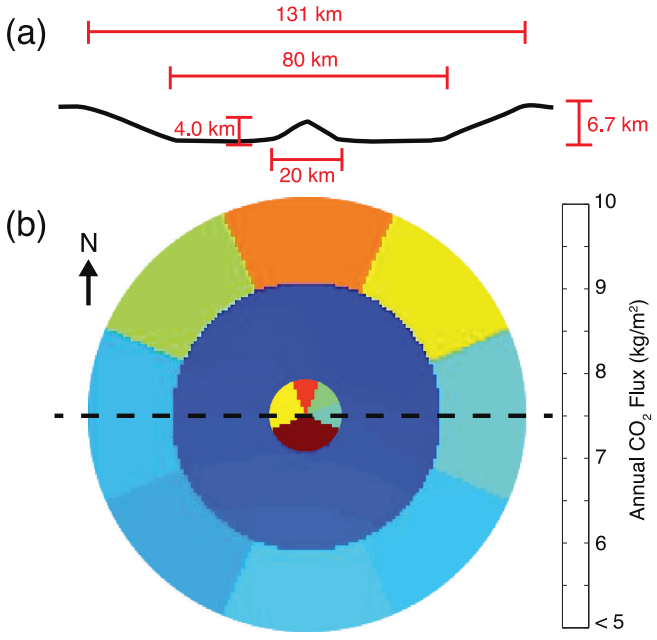

Fig. 10. (a) Topographic profile (vertically exaggerated × 3) through the center of our model's complex crater, such as the dashed line in (b). (b) Results showing the total CO_2 flux per m^2 in a complex crater of Wunda's size and location, for an initial condition of CO_2 everywhere on Umbriel's surface with the properties of regolith. We set the minimum flux on the color scale to be 5 kg/m^2 for clarity, but the south-facing slope of the central peak experiences flux as low as −2.4 kg/m^2. The crater floor is a CO_2 trap relative to the crater walls and central peak.

(~6 kg/m^2 or greater), even at the global minimum at the equator (Fig. 6). This is a consequence of the high obliquity of the Uranian system. However, the sublimation rate at low latitudes for a surface with the albedo and thermal inertia of CO_2 ice is very low, $\sim 3 \times 10^{-7}$ kg/m^2 each Uranian year (~84 terrestrial years). To understand whether this is sufficiently low to allow survival of a CO_2 deposit over long geologic time scales, we need to understand the CO_2 production rate and what happens to the molecules sublimated from the deposit.

To quantify these effects, we ran a simulation with an initial condition similar to an idealized present-day Umbriel. In this model, Umbriel is a sphere with no topography and the thermal properties of dark regolith everywhere, except at Wunda's location, where there is a complex crater with a bright annulus of CO_2 ice albedo and thermal inertia. We determined the fate of a sublimated CO_2 molecule under this condition. The molecule ballistically hops over time until it eventually returns to Wunda's CO_2 ice deposit or escapes Umbriel completely (because one of its hops exceeds escape velocity). We ran a Monte Carlo simulation of 10^5 sublimated molecules (we found that increasing the number of molecules does not significantly alter the following results). We find that ~15% of sublimated molecules eventually find their way back to Wunda, while ~85% escape the system via Jeans escape. Multiplying this percentage by the sublimation rate of the bright deposit and its area, we find that the entire area of Wunda loses a total of ~1200 kg of CO_2 ice every Uranian year (a little less than a m^3), for an average of 5×10^{-7} kg/s, or, equivalently, $\sim 1.6 \times 10^{-10}$ m of ablation every Uranian year. We estimate the minimum thickness of a CO_2 ice deposit that justifies our use of CO_2 thermal properties to be the annual skin depth, ~15 m. At this minimum thickness, the entire bright deposit has a mass of 2×10^{14} kg and therefore would persist over the age of the solar system even if it experiences no CO_2 replenishment.

This result has implications for the future evolution of Wunda's bright feature. If the source of detected CO_2 on Umbriel is radiolysis (Grundy et al., 2006; Cartwright et al., 2015), it may still be produced today. We ran the simulation described above for CO_2 particles starting at a random location on the trailing hemisphere, and found similar percentages of ~10% and ~90% for CO_2 molecules that deposit in Wunda and escape the system respectively. Thus, if Umbriel has a production rate $> 5 \times 10^{-6}$ kg/s (or in terms of per unit area, 10^{-18} kg m^{-2} s^{-1}), the Wunda deposit should be growing today.

4.2. Model uncertainties

Limited spacecraft data on Umbriel leads to uncertainty in our input parameters (Table 1). Our main qualitative result—that CO_2 ice is readily mobilized on Umbriel, migrating quickly to low latitudes, and stable over Gyr timescales if it accumulates in a single patch—is robust even though varying some of these parameters may change the resulting sublimation distribution. For example, we use an albedo of $A = 0.5$ for CO_2 ice, a value consistent with that observed for the bright feature in Wunda (Smith et al., 1986). However, reasonable albedos of CO_2 ice could range from 0.5–0.7 (Wood et al., 1971; Grundy et al., 2006), but the effect of an increased albedo would only increase the stability of CO_2 ice deposits further.

Our nominal thermal inertia value (970 J m^{-2} K^{-1} $s^{-0.5}$) for CO_2 assumes that the CO_2 deposit is in the form of solid, cohesive ice. Although we have shown sublimation is a slow process on Umbriel, grain growth is as well (Clark et al., 1983), leading to questions as to how long it would take radiolytically-produced CO_2 to form non-porous ice. However, thermal model results for the CO_2 deposit have a relatively low sensitivity to the exact thermal inertia value (Fig. 5). The maximum temperature of a CO_2 deposit during a Uranian year changes by only ~3 K as a result of varying thermal inertia within a large range of 300–1100 J m^{-2} K^{-1} $s^{-0.5}$ (the effect that this range has on sublimation rates is discussed in Section 2). We find that the key needed for stability of a CO_2 deposit over geologic time in Wunda is for the thermal inertia to be greater than that of Umbriel's regolith. The thermal inertia does not necessarily need to be so high that it represents a completely non-porous, cohesive slab of CO_2 ice.

There are a few effects not considered in our models. The one with the most potential importance is ultraviolet (UV) photolysis. UV radiation has to ability to dissociate CO_2 on airless body surfaces (e.g., Gerakines and Moore, 2001) into carbon monoxide and oxygen. While this effect has been estimated to be relatively rapid on the surface of Uranian satellites (Grundy et al., 2006), it remains unclear if UV dissociation is a dominant process in this context because it should not produce the observed planetocentric (more CO_2 on inner satellites) or longitudinal (more CO_2 on trailing hemispheres) trends (Cartwright et al., 2015). A possible counteracting factor is UV-induced CO_2 synthesis, in which absorption of photons by H_2O ice mixed with carbon-rich material produces CO_2 (e.g., Charakov et al., 2001). Laboratory experiments have shown that UV-irradiated cometary ice analogs can produce CO_2 and other compounds (Bernstein et al., 1995). Further study on this issue is warranted because such experiments were done at temperatures colder than the Uranian moons and because the penetration depths involved in UV-induced synthesis is different than that involved in radiolytic production (Delitsky and Lane, 1998). If the rate of UV dissociation is dominant over that of radiolytic production and/or UV synthesis, another source of CO_2 will need to be invoked.

Three neglected effects in our models are adsorption, Uranus-shine, and the possibility of changing orbital parameters. While adsorption of CO_2 molecules to regolith grains likely occurs to some degree, we model sublimation as the dominant process (e.g., Palmer and Brown, 2008). Adsorption will not affect the ultimate

fate of CO_2 molecules, only the time it takes an individual molecule to reach that fate (i.e., Jeans escape or caught in a low-latitude cold trap).

Uranus-shine is a minor effect because of Uranus' low energy balance (Pearl et al., 1990), which is perhaps due to the presence of thermal boundary layers in the planet's interior (Nettelmann et al., 2016). Approximating Uranus as a Lambert sphere, we integrate flux reflected toward Umbriel's sub-Uranian point and calculate it to be only 0.2% of the solar flux, a number that is a factor of ~20 too large for Wunda since it lies far from the center of the Uranus-facing hemisphere. Our models use the current orbital parameters and obliquity for Uranus and Umbriel, which we assume are representative of their long-term values. If these parameters change significantly over solar system history, the preferred locations of CO_2 ice deposition may change accordingly.

Our thermal models reveal that shadowing from crater walls and the central peak cools down the crater floor relative to other flat terrain. This effect is small: for the example in Fig. 10, Wunda's floor has a net CO_2 flux 8% greater than uncratered terrain at the same latitude. However, there is large uncertainty in crater dimensions, as we extrapolated depth and central peak height of a similar crater on Mimas. Because we extrapolate from the lower values given by Moore et al. (2004), our model crater depth (6.7 km) and central peak height (4 km) are likely underestimates. Our results on the effect that crater geometry has on CO_2 ice deposition are therefore conservative. The cooling effect on the crater floor should be stronger than our models predict (due to higher topography providing more shade), as should the warming effect on the walls and central peak. Increased thermal inertia at Wunda's location relative to other parts of Umbriel could also favor CO_2 deposition because it would suppress maximum temperatures and thus inhibit sublimation.

Grundy et al. (2003, 2006) & Cartwright et al. (2015) generated synthetic spectra in an attempt to estimate the quantity and nature of CO_2 needed to produce the telescopic observations. For Umbriel, the best fit mixture of Cartwright et al. (2015) involves ~8% of the surface area of the trailing hemisphere covered with a thin CO_2 layer. Wunda's bright deposit only represents ~1% of the surface area of the trailing hemisphere. It is possible that there are thus multiple solid CO_2 ice deposits similar to Wunda's contributing to the CO_2 detections. Indeed, our model as described does not favor Wunda over other equatorial craters with the same size and morphology in regards to CO_2 ice stability. We do not favor a scenario of multiple prominent solid CO_2 ice deposits within craters for two reasons. Firstly, other observed relatively bright areas in craters on Umbriel are far lower in albedo compared to Wunda's deposit (Helfenstein et al., 1989), and can be explained in a simpler way by excavation of less space-weathered material. Secondly, needing to invoke multiple bright deposits similar to Wunda's makes Voyager 2's observations of a single bright feature on a single Uranian satellite statistically unlikely (see Section 4.3).

Instead, we favor the case of Wunda being the only bright, solid, locally concentrated CO_2 ice deposit on Umbriel. It is possible that Wunda is preferred for deposition over other low-latitude craters because it is the one with the most favorable morphology, or because CO_2 is produced most strongly at the center of the trailing hemisphere (near Wunda's location). Although the ~8% surface area of Cartwright et al. (2015) is the best fit model based on spectra alone, it is not the only allowable model. Given the uncertainties involved, we argue that Wunda's deposit best fits the combination of the spectral observations and Voyager 2 image observations. We note that our favored scenario does not preclude radiolytic production; CO_2 mixed in with regolith grains outside of Wunda on the trailing hemisphere may still contribute to spectral detections.

4.3. Other uranian moons

CO_2 is detected on Ariel, Umbriel, Titania, and perhaps Oberon (Grundy et al., 2003, 2006, Cartwright et al., 2015), but only Umbriel has a feature as bright as Wunda's. If Wunda contains a CO_2 ice deposit, we require an explanation for why similar bright features are not seen on the other four major Uranian moons, a problem pointed out by Grundy et al., (2006). Smooth deposits on crater floors have been observed on Oberon (Helfenstein et al., 1991), but they are dark, both in an absolute sense and relative to the surrounding terrain, with albedos as low as ~0.05 (Smith et al., 1986). Broadly speaking, the two possibilities are: solid, bright, locally concentrated CO_2 ice deposits are not currently present on the surface of these other satellites, making Umbriel's feature a special case; or that such deposits are present on the other satellites but not yet observed, or obscured by sublimation lag.

There are plausible reasons to believe that CO_2 deposits do not exist on all of the other four large satellites despite the fact that imagery only exists for less than half their surfaces. The observations of (Grundy et al., 2006 & Cartwright et al., 2015) did not target Miranda, but if the radiolysis hypothesis is correct, CO_2 production should be greatest there as it is the innermost of the five large moons. However, we do not expect segregated CO_2 ice deposits on Miranda because of Jeans escape. Miranda's escape velocity of 193 m/s is far less than that of the other four moons. Comparing that value to expected velocity distributions of sublimated molecules on Uranian satellites (Fig. 7), it is clear Miranda would rapidly lose CO_2 to space, with ~50% of sublimated molecules escaping the system before even a single suborbital ballistic hop. In order to resist sublimation and atmospheric escape, any CO_2 on Miranda would need to be trapped as e.g. clathrates, as has been observed on other low mass moons (e.g., Clark et al., 2005). Similarly, all Uranian moons outside the classical five are also far too small to retain segregated CO_2. The next largest satellite, Puck, has an escape velocity of ~67 m/s (derived from measurements of Karkoschka (2001b)). This argument does not apply to Ariel, Titania, or Oberon, which have higher escape velocities than Umbriel.

CO_2 ice deposits are uncertain on Oberon. There is debate as to the presence of CO_2 detection on Oberon: (Grundy et al., 2006) did not report a successful detection from Oberon observations, while Cartwright et al. (2015) do argue for a statistically significant (though weak) detection. The weak detection may be the result of Oberon's distance from Uranus. Oberon spends part of its orbit outside the Uranian magnetic field, meaning that radiolytic production is weak because the only source of ions is the solar wind during that time. A similar argument has been made to show the minimal effect of radiolysis in producing CO_2 on Iapetus, which is outside Saturn's magnetic field entirely (Palmer and Brown, 2011). Thus, if CO_2 ice is present on Oberon, it may only be in a small quantity that is unable to accumulate in a single deposit and build up a higher albedo and thermal inertia relative to surrounding terrain.

Ariel has been observed to have at least a partially young surface with some degree of geologically-recent resurfacing (Smith et al., 1986; Plescia, 1987b; Zahnle et al., 2003), perhaps driven by tidal heating (Peale, 1988). It is possible that an ancient CO_2 ice deposit could be resurfaced by and buried under such extrusions. However, we do not find this explanation attractive since CO_2 ice is unambiguously identified on the present-day surface of Ariel (Grundy et al., 2003; Cartwright et al., 2015). Similarly, we have no explanation for why such a deposit would not exist on Titania.

Instead, we argue that CO_2 ice deposits likely exist on Ariel, Titania, and possibly Oberon, but have not yet been observed. Image coverage only spans a portion of the southern hemisphere on each of the five moons. Pictorial maps constructed by the U.S. Geological Survey (USGS) reveal that Umbriel is the only Uranian moon with

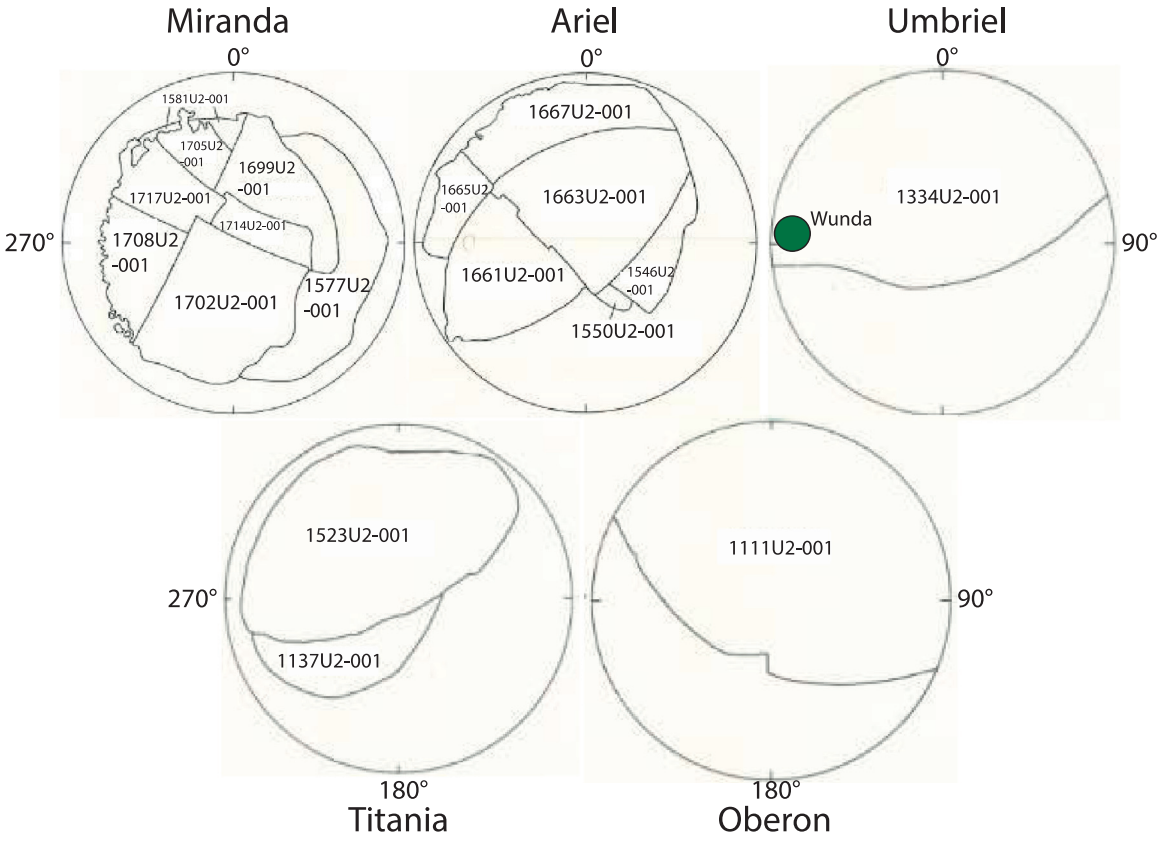

Fig. 11. USGS maps showing image coverage of the five major Uranian moons. Each large circle represents the southern hemisphere of the moon, and the labels show the longitude east; no moon has any significant coverage in the northern hemisphere. Outlined areas with an image number written inside represent areas of the moon that are covered. Small green circle represents the location of Wunda on Umbriel. Note that Umbriel is the only moon with coverage at the equator at the center of the trailing hemisphere (0° N, 270° E). (For interpretation of the references to colour in this figure legend, the reader is referred to the web version of this article.)

image coverage on the center of the trailing hemisphere (Fig. 11), which is the approximate location of Wunda. The USGS maps show that none of the five major satellites have significant coverage on their northern hemispheres. The latitude of Wunda is 7.9° S. If we assume that each of Ariel, Titania, Umbriel, and possibly Oberon has a bright CO_2 ice deposit, and that they are equally likely to be located at very low northern latitude as they are very low southern latitude, it is not surprising that we only have currently observed one of the three or four. If our hypothesis that Wunda contains a CO_2 ice deposit is correct, we predict full image coverage of all Uranian moons would reveal that Titania, Ariel, and possibly Oberon to have a similar low-latitude bright deposit, but not Miranda. We argue that ice is likely to be largely concentrated in one deposit, as observed on high-obliquity Pluto (Stern et al., 2015; Grundy et al., 2016) and suggested by the longitudinal preference of CO_2 on Uranian moons (Grundy et al., 2006; Cartwright et al., 2015), but further observations are needed to determine if multiple deposits of similar size could be plausible.

The spectroscopic analysis of Ariel (Grundy et al., 2003, 2006; Cartwright et al., 2015) indicate a larger abundance of CO_2 there. Therefore, if our reasoning above is correct, the bright CO_2 ice deposit we hypothesize for Ariel likely must be larger than a feature that can fit inside a complex crater of Wunda's size. One possibility is that ice is simply concentrated into an impact basin that is significantly larger than Wunda. Alternatively, Ariel's highly tectonized terrain is dominated by long canyons (Smith et al., 1986), and may play a role. One or more canyons mantled by CO_2 deposits may explain the wider range of longitudes that are suggested to contain CO_2 by the spectroscopic detections (Grundy et al., 2003, 2006; Cartwright et al., 2015).

4.4. Alternatives to ballistically transported CO_2 ice

Alternative explanations for Wunda's bright feature are less attractive than our CO_2 ice deposit hypothesis. Impact crater ejecta can be bright relative to Umbriel's dark surface (Helfenstein et al., 1989), but should not reside within the crater itself. Cryovolcanism has been suggested as a possible source of CO_2 on Uranian satellites in addition to radiolytic production (Cartwright et al., 2015), and Wunda has specifically been mentioned as possibly housing a cryovolcanic deposit (Plescia, 1987a). However, early endogenic resurfacing on Umbriel is expected to involve dark material (albedo ~0.1) (Helfenstein et al., 1989), and later endogenic activity is not expected (Peale, 1988). The expectation of dark extrusions is strengthened by observations of smooth deposits in craters on Oberon that are interpreted as extrusive (Helfenstein et al., 1991), but are darker than the surrounding terrain and have low albedo (as low as ~0.05).

Another argument against extrusive CO_2 in Wunda concerns the uniformly dark nature of Umbriel's surface. It has been suggested that this unusual surface is the result of a blanketing of low-albedo material (Smith et al., 1986). If this hypothesis is correct, the superposed bright material in Wunda would need to be younger, but late-stage endogenic activity is unlikely on Umbriel based on analysis of crater distributions (Plescia, 1987a) and orbital histories (Peale, 1988). Extrusive CO_2 would be more plausible if instead the homogenous dark surface was representative of Umbriel's upper crust, which would allow endogenic activity superposed on that dark surface to be ancient.

Whatever the nature of Umbriel's dark material, it is possible brighter material may be excavated from depth via impacts. Of par-

ticular interest here is that CO_2 has been suggested to be excavated by impacts on Callisto (Hibbitts et al., 2002). Hibbitts et al., (2002) interpreted the detected CO_2 on Callisto as being sourced from CO_2 clathrates because segregated CO_2 is predicted to be thermally unstable on surfaces in the Jupiter system, but CO_2 ice could be thermally stable in the Uranian system (Lebofsky, 1975). Because Umbriel has craters larger than Wunda (Malingee and Wokolo) that do not contain similarly bright deposits, and because excavated CO_2 should be associated with crater ejecta as well as within the crater itself (as seen on Callisto), we argue that the bright material inside Wunda is unlikely to represent a direct excavation of CO_2. However, large impacts on Umbriel could excavate CO_2 that later migrates to Wunda; this process provides an additional source of CO_2 to complement radiolytic production at the present-day surface.

Ices other than CO_2 are worth considering as constituents of Wunda's bright deposit. Nitrogen ice deposits have been observed on Pluto (Stern et al., 2015) and may exist on the surface of Neptune's moon Triton (e.g., Hansen and Paige, 1992). Although N_2 ice has bright albedo similar to CO_2 ice, it sublimates at too low temperatures to be stable on Uranus' warmer moons throughout even one Uranian year. Jeans escape is also more important for N_2 ice compared to CO_2 ice because of its lower molecular mass. We estimate, based on Eq. 5 and our thermal model results, that ~2% of sublimated N_2 molecules will immediately escape Umbriel, over an order of magnitude greater than that of CO_2 (< 0.1%). This escape rate is too high for N_2 to accumulate on Umbriel's surface. Even if a single deposit of N_2 ice the size of Wunda's bright patch did form, we find (using the same exercise described in Section 4.1 for CO_2 molecules) that > 98% of N_2 molecules sublimated from such an ice patch escape Umbriel.

Carbon monoxide and methane ices have also been detected on Pluto, sometimes appearing in crater floors (Stern et al., 2015; Grundy et al., 2016). CO has a similarly high escape percentage of sublimated molecules as N_2, and methane ice or ammonia ice would have a much greater one (> 10%, due to their lower molecular masses). Ultimately, the mass of Umbriel ($\sim 1.2 \times 10^{21}$ kg) is potentially high enough to retain a CO_2 ice deposit over Gyr timescales, but not a deposit composed of the other ices found in the outer solar system.

H_2O ice has a low molecular mass compared to CO_2, but is not volatile at temperatures relevant for Uranus, so the above argument concerning Jeans escape does not apply. Water ice composes a majority of Umbriel's mass, so it is worth considering the possibility that Wunda exposes a bright Umbrielian crust beneath its dark surface. However, larger, and presumably deeper (Schenk, 1989), craters do not expose similar bright spots. Additionally, while more study is needed to precisely quantify the effects of space weathering on the Uranian satellites, it seems clear that charged particle irradiation would darken nearly-pure H_2O deposits on Umbriel on geologically fast timescales (Thompson et al., 1987). In contrast, a CO_2 ice deposit could maintain a bright appearance via the addition of new radiolytically produced CO_2 molecules that superpose older CO_2 ice that has been darkened by space weathering effects.

5. Conclusions

We conclude based on our thermal and ballistic transport modeling, combined with Voyager 2 observations, that the bright feature inside Wunda is likely a deposit of CO_2 ice. There are several lines of evidence supporting this idea. (1) CO_2 ice has been detected on the trailing hemisphere of Umbriel (Grundy et al., 2006; Cartwright et al., 2015), and Wunda lies very near the center of the trailing hemisphere. (2) Our thermal and ballistic transport models show CO_2 ice migrates to low latitudes over geologically short timescales, and Wunda lies nearly at the equator. (3) Umbriel occupies a "sweet spot" in regards to CO_2 volatility: it is warm enough for CO_2 on regolith to be mobilized via sublimation for migration to cold traps, but cold enough such that a pure sequestered CO_2 surface deposit is largely resistant to sublimation, and cold and massive enough to prevent most sublimated CO_2 from escaping via Jeans escape. Our thermal models show that a CO_2 ice deposit, once accumulated sufficiently to alter its local region's albedo and thermal inertia from that of Umbriel's dark regolith to that of CO_2 ice, can survive over the age of the solar system. (4) The observed albedo of the bright feature in Wunda Smith et al., 1986) is consistent with the albedo of CO_2 ice (Wood et al., 1971). ((5) Wunda is likely a complex crater with a central peak, which provides a plausible explanation for the annular shape of the bright floor deposit due to surface slope and shadowing effects.

Lines of evidence (1), (2), and (3) also apply to Ariel, Titania, and Oberon, although Miranda is likely insufficiently massive to retain CO_2 ice over geologically long timescales. Therefore, our results and analyses suggest that similar CO_2-filled complex craters could be present on Ariel, Titania, and Oberon. Such craters may simply be undiscovered because of the sparse imaging coverage of these moons by Voyager 2 during its flyby. We note that Umbriel is the only moon of these five major satellites where coverage exists at the center of the trailing hemisphere, where Wunda is located. Our results and analyses support the hypothesis that the bright annulus in Wunda is composed of CO_2 ice. Subsequent high resolution telescopic observations and/or another spacecraft mission to the Uranian system (Arridge et al., 2014) are needed to further investigate Umbriel's anomalously bright deposit.

Acknowledgements

We thank the Voyager 2 imaging science system team for collecting data on the Uranian system that is still bearing fruit 30 years after the fly-by, and Drs. Eriksson and McGasket for their inspiration throughout this project. We thank Richard Cartwright and Eric E. Palmer for their comments which greatly improved the quality of this paper.

Appendix A

This Appendix provides derivations for calculating the horizon heights of the rim (Appendix A.1) and central peak (Appendix A.2) of a complex crater relative to an observer standing on the crater floor. The final equations are Eqs. 1 and 2 in the main text. Figs. A1 and A2 provide visual aid for the calculations of horizon heights for the crater rim and central peak, respectively.

A.1. Horizon height: crater rim

Assume an observer is standing on the floor of a complex crater of rim-to-rim diameter D and rim-to-floor depth d at a distance x from the center of the crater (Fig. A1). The observer is located at an angle φ, measured clockwise from due north, and is facing direction β measured in the same way. The lateral distance y between the observer and the crater rim is related to the observer's position by the cosine rule:

$$\left(\frac{D}{2}\right)^2 = x^2 + y^2 - 2xy\cos(\pi - \varphi + \beta) \tag{A1}$$

Rearranged as a function of y, Eq. A1 becomes:

$$y^2 - [2x\cos(\pi - \varphi + \beta)]y + \left[x^2 - \left(\frac{D}{2}\right)^2\right] = 0 \tag{A2}$$

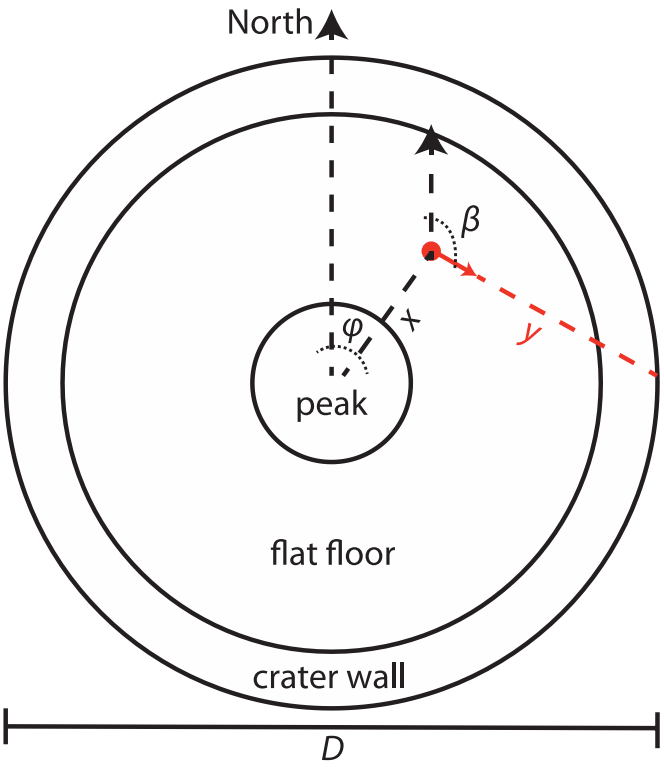

Fig. A1. Diagram showing relevant variables for calculation of the horizon height of the crater rim, H_{rim}. The red dot is the location of the observer on the crater floor, and the red arrow points in the direction they are facing. See text S1 for explanation of the variables. (For interpretation of the references to colour in this figure legend, the reader is referred to the web version of this article.)

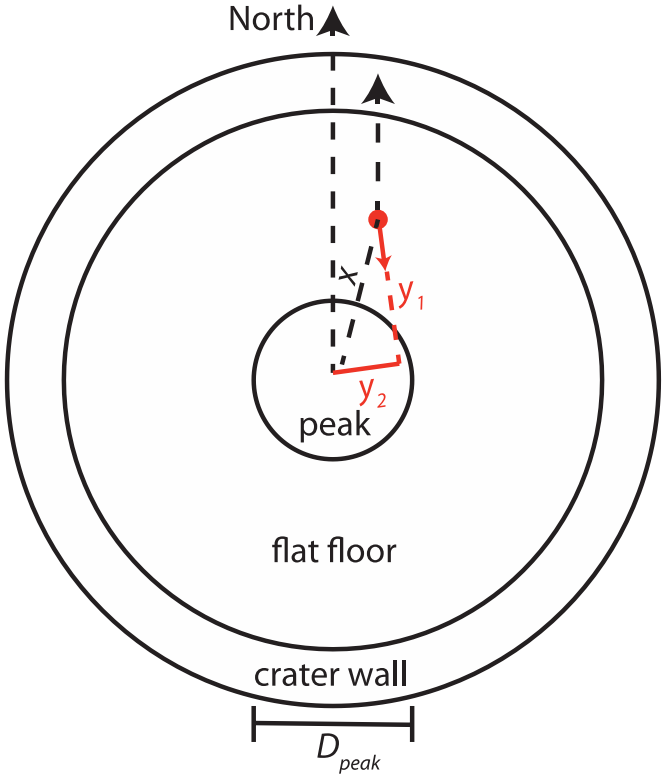

Fig. A2. Diagram showing relevant variables for calculation of the horizon height of the central peak, H_{peak}. The red dot is the location of the observer on the crater floor, and the red arrow points in the direction they are facing. See text S2 for explanation of the variables. Angles φ and β are omitted for clarity, but represent the same angles as shown in Figure S1.

We can now use the quadratic equation to obtain solutions for y:

$$y = x\cos(\pi - \varphi + \beta) \pm \sqrt{x^2\cos^2(\pi - \varphi + \beta) - x^2 + \left(\frac{D}{2}\right)^2} \quad \text{(A3)}$$

Note that because the crater radius ($D/2$) is always greater than x, the expression inside the square root is always positive and thus the solutions for x are always real. Eq. A3 can be rearranged by factoring out x^2 from inside the square root, using Pythagorean trigonometric identities, and choosing the positive root so that the y is positive:

$$y = x\left[\cos(\pi - \varphi + \beta) + \sqrt{\left(\frac{D}{2x}\right)^2 - \sin^2(\pi - \varphi + \beta)}\right] \quad \text{(A4)}$$

The horizon height of the rim is simply:

$$H_{rim} = \arctan\left(\frac{d}{y}\right) \quad \text{(A5)}$$

Combining Eqs. A4 and A5, this becomes:

$$H_{rim} = \arctan\left[\frac{d}{x} \times \frac{1}{\cos(\pi - \varphi + \beta) + \sqrt{\left(\frac{D}{2x}\right)^2 - \sin^2(\pi - \varphi + \beta)}}\right] \quad \text{(A6)}$$

A.2. Horizon height: central peak

Assume an observer is standing on the floor of a complex crater with central peak diameter D_{peak} and central peak height h_{peak} at a distance x from the center of the crater (Fig. A2). The observer is located at an angle φ, measured clockwise from due north, and is facing direction β measured the same way. The lateral distance y_1 between the observer and the highest point of the central peak in the direction the observer is facing is given by:

$$y_1 = x\cos(|\pi - \beta + \varphi|) \quad \text{(A7)}$$

Similarly, the lateral distance y_2 between the center of the central peak and highest point of the central peak in the direction the observer is facing is given by:

$$y_2 = x\sin(|\pi - \beta + \varphi|) \quad \text{(A8)}$$

The height of that point on the central peak, z, assuming the peak is in the shape of a cone (i.e., has uniform slope) is:

$$z = h_{peak}\left(1 - \frac{2y_2}{D_{peak}}\right) \quad \text{(A9)}$$

The horizon height of the rim is:

$$H_{peak} = \arctan\left(\frac{z}{y_1}\right) \quad \text{(A10)}$$

Combining Eqs. A7–A10, this becomes:

$$H_{peak} = \arctan\left(\frac{h_{peak}}{D_{peak}} \times \frac{D_{peak} - 2x\sin(|\pi - \beta + \varphi|)}{x\cos(|\pi - \beta + \varphi|)}\right) \quad \text{(A11)}$$

References

Arridge, C.S., Achilleos, N., Agarwal, J., et al., 2014. The science case for an orbital mission to Uranus: exploring the origins and evolution of ice giant planets. Planet. Space Sci. 104, 122–140.

Azreg-Aïnou, M., 2005. Low-temperature data for carbon dioxide. M. Monatsh. Chem. 136, 2017–2027.

Banks, M.E., Byrne, S., Galla, K., McEwen, A.S., Bray, V.J., Dundas, C.M., Fishbaugh, K.E., Herkenhoff, K.E., Murray, B.C., 2010. Crater population and resurfacing of the Martian north polar layered deposits. J. Geophys. Res. 115, E08006.

Bauer, J.M., Roush, T.L., Geballe, T.R., 2002. The near infrared spectrum of Miranda: evidence of crystalline water ice. Icarus 158, 178–190.
Bernstein, M.P., Sandford, S.A., Allamandola, L.J., Chang, S., Scharberg, M.A., 1995. Organic compounds produced by photolysis of realistic interstellar and cometary ice analogs containing methanol. Astrophys. J. 454, 327–344.
Bray, V.J., Collins, G.S., Morgan, J.V., Schenk, P.M., 2008. The effect of target properties on crater morphology: comparison of central peak craters on the Moon and Ganymede. Meteoritics Planet. Sci. 43, 1979–1992.
Buratti, B., Wong, F., Mosher, J., 1990. Surface properties and photometry of the Uranian satellites. Icarus 84, 203–214.
Butler, B.J., 1997. The migration of volatiles on the surfaces of Mercury and the Moon. J. Geophys. Res. Planets 102, 19283–19291.
Cartwright, R.J., Emery, J.P., Rivkin, A.S., Trilling, D.E., Pinilla-Alonso, N., 2015. Distribution of CO_2 ice on the large moons of Uranus and evidence for compositional stratification of their near-surfaces. Icarus 257, 428–456.
Chakarov, D.V., Gleeson, M.A., Kasemo, B., 2001. Photoreactions of water and carbon at 90 K. J. Chem. Phys. 115, 9477–9483.
Clark, R.N., Fanale, F.P., Zent, A.P., 1983. Frost grain size metamorphism: implications for remote sensing of planetary surfaces. Icarus 56, 233–245.
Clark, R.N., Lucey, P.G., 1984. Spectral properties of ice-particulate mixtures and implications for remote sensing: 1. intimate mixture. J. Geophys. Res. Solid Earth 89, 6341–6348.
Clark, R.N., Brown, R.H., Jaumann, R., et al., 2005. Compositional maps of Saturn's moon Phoebe from imaging spectroscopy. Nature 435, 66–69.
Crank, J., Nicolson, P., 1947. A practical method for numerical evaluation of solutions of partial differential equations of the heat-conduction type. Proc. Camb. Phil. Soc. 43, 50–67.
Delitsky, M.L., Lane, A.L., 1998. Ice chemistry on the Galilean satellites. J. Geophys. Res. Planets 103, 31391–31403.
Earle, A.M., Binzel, R.P., Young, L.A., Stern, S.A., Ennico, K., Grundy, W., Olkin, C.B., Weaver, H.A.the New Horizons Geology and Geophysics Imaging Team, 2016. Long-term surface temperature modeling of Pluto. Icarus in press.
Escribano, R.M., Muñoz Caro, G.M., Cruz-Diaz, G.A., Rodríguez-Lazcano, Y., Maté, B., 2013. Crystallization of CO_2 ice and the absence of amorphous CO_2 ice in space. PNAS 110, 12899–12904.
Feldman, W.C., Maurice, S., Binder, A.B., Barraclough, B.L., Elphic, R.C., Lawrence, D.J., 1998. Fluxes of fast and epithermal neutrons from Lunar Prospector: Evidence for water ice at the lunar poles. Science 281, 1496–1500.
Gerakines, P.A., Moore, M.H., 2001. Carbon suboxide in astrophysical ice analogs. Icarus 154, 372–380.
Gomis, O., Strazzulla, G., 2005. CO_2 production by ion irradiation of H_2O ice on top of carbonaceous materials and its relevance to the Galilean satellites. Icarus 177, 570–576.
Gourgeot, F.C., Dumas, F., Merlin, P., Vernazza, Alvarez-Candal, A, 2014. Near-infrared spectroscopy of Miranda. Astron. Astrophys. 562, A46.
Grundy, W.M., Buie, M.W., Stansberry, J.A., Spencer, J.R., Schmitt, B., 1999. Near-infrared spectra of icy outer solar system surfaces: remote determination of H_2O ice temperatures. Icarus 142, 536–549.
Grundy, W.M., Young, L.A., Young, E.F., 2003. Discovery of CO_2 ice and leading–trailing spectral asymmetry on the uranian satellite Ariel. Icarus 162, 222–229.
Grundy, W.M., Young, L.A., Spencer, J.R., Johnson, R.E., Young, E.F., Buie, M.W., 2006. Distributions of H_2O and CO_2 ices on Ariel, Umbriel, Titania, and Oberon from IRTF/SpeX observations. Icarus 184, 543–555.
Grundy, W.M., Binzel, R.P., Buratti, B.J., et al., 2016. Surface compositions across Pluto and Charon. Science 351, 1283.
Hanel, R., Conrath, B., Flaser, F.M., Kunde, V., Maguire, W., Pearl, J., Pirraglia, J., Samuelson, R., Cruikshank, D., Gautier, D., Gierasch, P., Horn, L., Schulte, P., 1986. Infrared observations of the Uranian system. Science 233, 70–74.
Hansen, C.J., Paige, D.A., 1992. A thermal model for the seasonal nitrogen cycle on Triton. Icarus 99, 273–288.
Helfenstein, P., Thomas, P.C., Veverka, J., 1989. Evidence from Voyager II photometry for early resurfacing of Umbriel. Nature 338, 324–326.
Helfenstein, P., Hillier, J., Weitz, C., Veverka, J., 1991. Oberon: color photometry from Voyager and its geological implications. Icarus 90, 14–29.
Hibbitts, C.A., Klemaszewski, J.E., McCord, T.B., Hansen, G.B., Greeley, R., 2002. CO_2-rich impact craters on Callisto. J. Geophys. Res. 107, E105084.
Howett, C.J.A., Spencer, J.R., Pearl, J., Segura, M., 2010. Thermal inertia and bolometric Bond albedo values for Mimas, Enceladus, Tethys, Dione, Rhea and Iapetus as derived from Cassini/CIRS measurements. Icarus 206, 573–593.
Jankowski, D.G., Squyres, S.Q., 1988. Solid-state ice volcanism on the satellites of Uranus. Science 241, 1322–1325.
Karkoschka, E., 2001a. Comprehensive photometry of the rings and 16 satellites of Uranus with the Hubble Space Telescope. Icarus 151, 51–68.
Karkoschka, E., 2001b. Voyager's eleventh discovery of a satellite of Uranus and photometry and the first size measurements of nine satellites. Icarus 151, 69–77.
Krimigis, S.M., Armstrong, T.P., Axford, W.I., Cheng, A.F., Gloeckler, G., Hamilton, D.C., Keath, E.P., Lanzerotti, L.J., Mauk, B.H., 1986. The magnetosphere of Uranus: hot plasma and radiation environment. Science 233, 97–102.
Lane, A.L., Nelson, R.M., Matson, D.L., 1981. Evidence for sulphur implantation in Europa's UV absorption band. Nature 292, 38–39.
Lebofsky, L.A., 1975. Stability of frosts in the solar system. Icarus 25, 205–217.
McCord, T.B., Li, J.-Y., Combe, J.-P., et al., 2012. Dark material on Vesta from the infall of carbonaceous volatile-rich material. Nature 491, 83–86.
Moore, J.M., Schenk, P.M., Bruesch, L.S., Asphaug, E., McKinnon, W.B., 2004. Large impact features on middle-sized icy satellites. Icarus 171, 421–443.
Ness, N.F., Acuña, M.H., Behannon, K.W., Burlaga, L.F., Connerney, J.E.P., Lepping, R.P., Neubauer, F.M., 1986. Magnetic fields at Uranus. Science 233, 85–89.
Nettelmann, N., Wang, K., Fortney, J.J., Hamel, S., Yellamilli, S., Bethkenhagen, M., Redmer, R., 2016. Uranus evolution models with simple thermal boundary layers. Icarus 275, 107–116.
Neumann, G.A., Cavanaugh, J.F., Sun, X., Mazarico, E.M., Smith, D.E., Zuber, M.T., Mao, D., Paige, D.A., Solomon, S.C., Ernst, C.M., Barnouin, O.S., 2013. Bright and dark deposits on Mercury: evidence for surface volatiles. Science 339, 296–300.
Palmer, E.E., Brown, R.H., 2008. The stability and transport of carbon dioxide on Iapetus. Icarus 195, 434–446.
Palmer, E.E., Brown, R.H., 2011. Production and detection of carbon dioxide on Iapetus. Icarus 212, 807–818.
Peale, S.J., 1988. Speculative histories of the Uranian satellite system. Icarus 74, 153–171.
Pearl, J.C., Conrath, B.J., Hanel, R.A., Pirraglia, J.A., Coustenis, A., 1990. The albedo, effective temperature, and energy balance of Uranus as determined from Voyager IRIS data. Icarus 84, 12–28.
Plescia, J.B., 1987a. Cratering history of the Uranian satellites: Umbriel, Titania, and Oberon. J. Geophys. Res. 92, 14918–14932.
Plescia, J.B., 1987b. Geological terrains and crater frequencies on Ariel. Nature 327, 201–204.
Rayner, J.T., Toomey, D.W., Onaka, P.M., et al., 2003. SpeX: a medium-resolution 0.8–5.5 μ spectrograph and imager for the NASA infrared telecscope facility. Astron. Soc. Pacific 115.
Schenk, P.M., 1989. Crater formation and modification on the icy satellites of Uranus and Saturn: depth/diameter and central peak occurrence. J. Geophys. Res. 94, 3813–3832.
Smith, B.A., Soderblom, L.A., Beebe, R., et al., 1986. Voyager 2 in the Uranian system: imaging science results. Science 233, 43–64.
Soifer, B.T., Neugebauer, G., Matthews, K., 1981. Near-infrared spectrophotometry of the satellies and rings of Uranus. Icarus 45, 612–617.
Stern, S.A., Bagenal, F., Ennico, K., et al., 2015. The Pluto system: Initial results from its exploration by New Horizons. Science 350, aad1815–aad1817.
Stone, E.C., Cooper, J.F., Cummings, A.C., McDonald, F.B., Trainor, J.H., Lal, N., Mcquire, R., Chenette, D.L., 1986. Energetic charged particles in the Uranian magnetosphere. Science 233, 93–97.
Sumarokov, V.V., Stachowiak, P., Jezowski, A., 2003. Low-temperature thermal conductivity of solid carbon dioxide. Low Temp. Phys. 29, 449–450.
Teolis, B.D., Jones, G.H., Miles, P.F., Tokar, R.L., Magee, B.A., Waite, J.H., Roussos, E., Young, D.T., Crary, F.J., Coates, A.J., Johnson, R.E., Tseng, W.-L., Baragiola, R.A., 2010. Cassini finds an oxygen-carbon dioxide atmosphere at Saturn's icy moon Rhea. Science 330, 1813–1815.
Teolis, B.D., Waite, J.H., 2016. Dione and Rhea seasonal exospheres revealed by Cassini CAPS and INMS, Cassini finds an oxygen-carbon dioxide atmosphere at Saturn's icy moon Rhea. Icarus 272, 277–289.
Thompson, W.R., Murray, B.G.J.P.T., Khare, B.N., Sagan, C., 1987. Coloration and darkening of methane clathrate and other ices by charged particle irradiation: Applications to the outer solar system. J. Geophys. Res. Space Phys. 92, 14933–14947.
Veverka, J., Thomas, P., Helfenstein, P., Brown, R.H., Johnson, T.V., 1987. Satellites of Uranus: disk-integrated photometry from Voyager imaging observations. J. Geophys. Res. Space Phys. 92, 14895–14904.
Wood, B.E., Smith, A.M., Roux, J.A., Seiber, B.A., 1971. Spectral absolute reflectance of CO_2 frosts from 0.5 to 12.0μ. AIAA Journal 9, 1338–1344.
Zahnle, K., Schenk, P., Levison, H., Dones, L., 2003. Cratering rates in the outer solar system. Icarus 163, 263–289.